ADVANCED MATERIALS TECHNOLOGIES
www.advmattechnol.de

A Wearable Self-Powered Multi-Parameter Respiration Sensor

Jieyu Dai, Jianping Meng, Xiaoming Zhao, Weiyi Zhang, Yubo Fan, Bojing Shi,* and Zhou Li**

Respiratory disease can be early warned by many respiratory parameters such as intensity, rhythm, temperature, and breath molecules like acetone. It requires a complex process to measure these respiratory parameters simultaneously in clinical practice. Therefore, it is a hot topic to design portable devices especially wearable electronics to monitor respiratory conditions continually in daily life. Here, a flexible self-powered multi-parameter respiration sensor based on poly(vinylidene fluoride) (PVDF) thin film and flexible interdigital electrodes that is bonding with sodium-doped zinc oxide nanoflowers is demonstrated , which can detect airflow, temperature, and acetone during breathing. The respiration sensor may provide some reference ways for the fabrication of miniaturized respiratory disease monitoring devices.

1. Introduction

Respiration, as an uninterrupted and vital biomechanical behavior that continues throughout human life, contains a wealth of physiological information. A respiratory analysis is a rapid, non-invasive, painless, low-cost, and convenient method of early disease diagnosis and real-time physiological monitoring.[1] For example, assessing diaphragmatic movements during breathing can identify abnormal apnoea, asthma, cardiac arrest, and lung cancer, among other human diseases, at an early stage.[2] Besides, exhaled gases are a mixture of up to 1800 different chemicals, including carbon dioxide, nitrogen, oxygen, water vapor, and volatile organic components (VOCs).[3] The composition and concentration of exhaled breath can be used as biomarkers, providing a wealth of biochemical and physiological information in disease diagnosis and early intervention.[4] Nowadays, scientists have found that some VOCs are strongly correlated with certain diseases, which include: ammonia as a biomarker for kidney disease, ethanol can be seen as an indicator of cirrhosis, methane breath testing can identify small intestinal bacterial overgrowth (SIBO), and acetone concentration be considered an important indicator of the diabetic disease.[5]

Common respiration sensors include physical signal collection devices such as strain gauge sensors, temperature sensors and flow sensors, and molecular signal acquisition devices such as quartz crystal microbalances, gas chromatography, and chemoreceptive sensors, etc.[6] These sensors have relatively reliable performance in respiratory signal detection, but most rely on external power sources, which are large and rigid, hindering their potential for widespread use in biomedical devices.[2,7] To realize the daily monitoring of the biomedical signals related to respiratory diseases in real time, researchers

J. Dai, J. Meng, W. Zhang, Z. Li
Beijing Institute of Nanoenergy and Nanosystems
Chinese Academy of Sciences
Beijing 101400, China
E-mail: zli@binn.cas.cn

J. Dai, Y. Fan, B. Shi
Key Laboratory for Biomechanics and Mechanobiology of Ministry of Education
Beijing Advanced Innovation Center for Biomedical Engineering
School of Biological Science and Medical Engineering
School of Engineering Medicine
Beihang University
Beijing 100191, China
E-mail: yubofan@buaa.edu.cn; bjshi@buaa.edu.cn

J. Dai
Central Laboratory
Affiliated Dongguan Hospital
Southern Medical University
Dongguan 523058, China

X. Zhao
Maternal and Child Health Hospital of Hubei Province
Wuhan 430070, China

Z. Li
School of Nanoscience and Technology
University of Chinese Academy of Sciences
Beijing 100049, China

Z. Li
Center on Nanoenergy Research
School of Physical Science and Technology
Guangxi University
Nanning 530004, China

Z. Li
Institute for Stem Cell and Regeneration
Chinese Academy of Sciences
Beijing 100101, China

The ORCID identification number(s) for the author(s) of this article can be found under https://doi.org/10.1002/admt.202201535.

DOI: 10.1002/admt.202201535

have designed some wearable devices such as smart masks[8] and sensors attached around the chest.[9] These devices may continuously measure vital parameters, thus helpful in tracking the progression of respiratory diseases. However, wearable multiplexed sensor systems are currently formed from some relatively independent elements, still subject to the volume and life of a battery, and need to develop miniaturization and integration in the future. A possible way to overcome the battery challenge is to harvest energy from the body and its surroundings, including biomechanical, solar, thermal, and biochemical energy, so that the device can operate in a self-powered way.[10] In recent years, researchers have developed quite a few self-powered respiratory sensing systems, the electrical signals they output are closely related to the respiratory parameters.[11] For example, piezoelectric nanogenerators (PENGs) can be used to collect mechanical signals from thoracic/abdominal heaving and respiratory airflow, the combination of gas-sensitive materials with TENGs for VOCs signal acquisition, and pyroelectric nanogenerators (PyNGs) to collect respiratory temperature signals.[12] These self-powered respiration sensors are free from dependence on external power sources, but most of them still have defects like collecting relatively single respiratory signals.

Here, we designed a flexible self-powered multi-parameter respiration sensor (SMRS) for respiratory monitoring based on the combination of poly(vinylidene fluoride) (PVDF) thin film and gas-sensitive material. This sensing system can be easily combined with respiratory-related wearable devices such as face masks, where the respiratory airflow drives the PENG while temperature changes drive the PyNG to produce a corresponding output signal and detect the acetone concentration in the exhaled gas (**Figure 1**a). The piezoelectricity of the PVDF that makes up the PENG converts the mechanical energy generated during exhalation and inhalation into electrical energy and outputs signals corresponding to different breathing patterns. At the same time, the pyroelectric effect of PVDF allows the output of signals corresponding to temperature changes. In combination with gas-sensitive material such as sodium-doped zinc oxinde (Na:ZnO) nanoflowers (NFs), the device can monitor acetone concentrations in exhaled breath, providing a new idea for the early diagnosis of diseases such as diabetes.

2. Results and Discussion

The 3D constitutional diagram of the SMRS can be seen in Figure 1b, in which the PVDF with silver electrodes mainly works as the piezoelectric part and pyroelectric part. Furthermore, the gold interdigital electrodes covered with gas-sensitive materials can realize the acetone concentration detection of human exhaled gas. The whole structure and each component are in good flexibility (Figure 1c,d), which means the SMRS can be integrated with human breath collectors such as medical masks conveniently, thus harvesting corresponding respiratory signals.

2.1. Working Mechanism and Performance of Piezoelectric Part of SMRS

Due to the piezoelectric effect, and lightweight, little size, superior flexibility of the PVDF thin film, it can be easily driven by bending or twisting.[13] Human inhalation and exhalation would cause a change in the airflow, and this change could drive the SMRS based on PENG to collect respiratory-related signals. The working mechanism of the PVDF-based PENG is shown in **Figure 2**a. In the crystal structure of PVDF, there is a balance

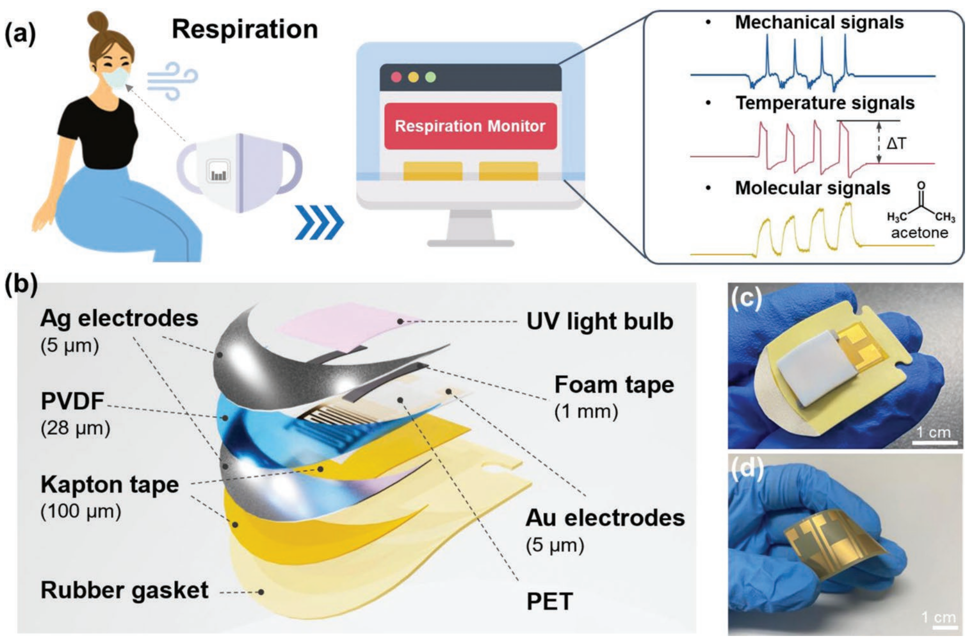

Figure 1. Schematic illustrations of the multi-parameter respiration monitoring system. a) Diagram of the working process of the respiration monitoring system collecting mechanical signals, temperature signals, and molecular signals. b) 3D constitutional diagram. c) Photograph of the SMRS. d) Photograph of flexible interdigital electrodes on PET film.

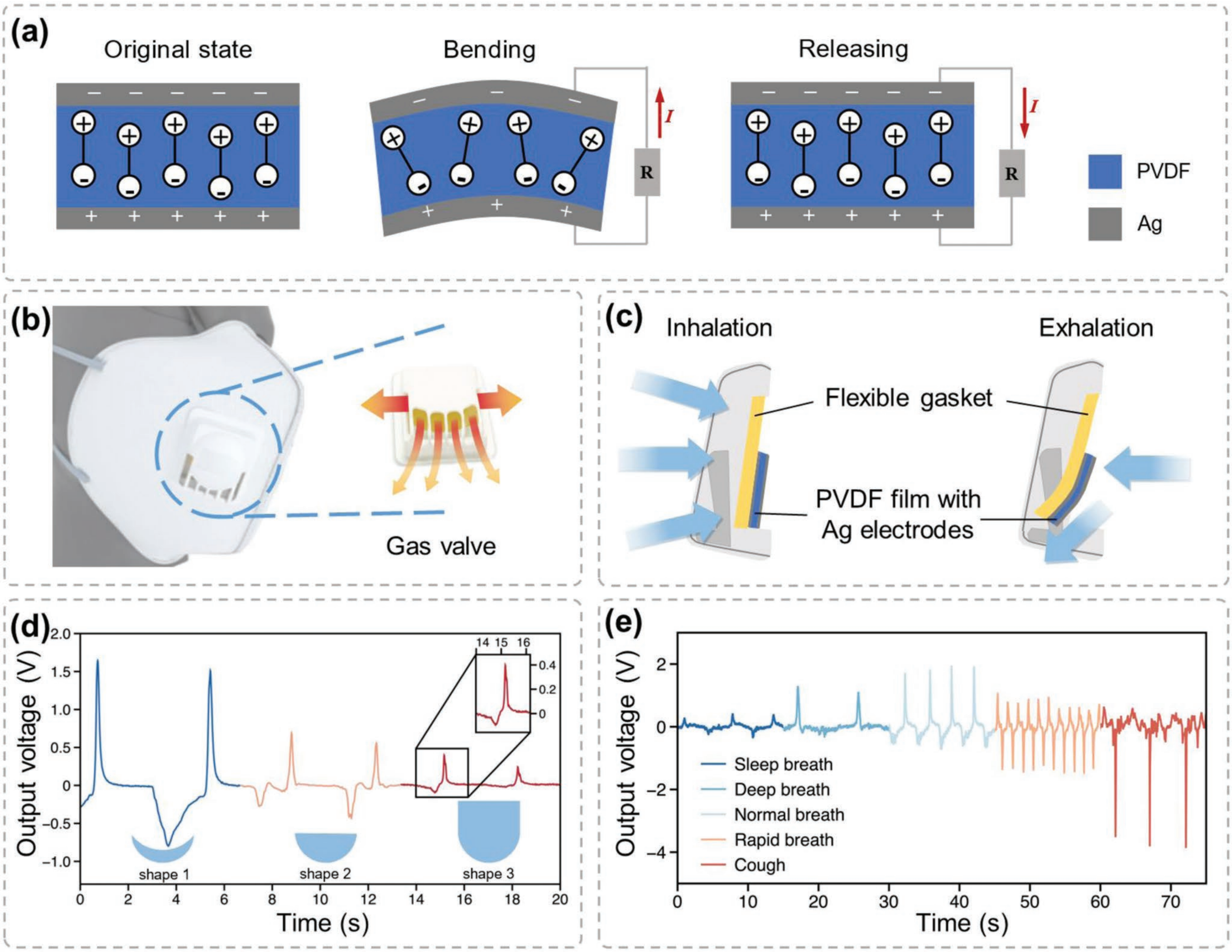

Figure 2. Working mechanism and output performance of the PENG based on the PVDF film. a) Principles of the PVDF-based PENG in the bending/releasing mode. b) Schematic diagram of the gas valve on the face mask. c) Schematic diagram of the PENG combined with the gas valve. d) Output voltage of respiratory mechanics signals collected by different shapes of PENG. e) Respiratory mechanics signals collected by PENG in different breathing modes.

between positive and negative charges, which remain neutral on the virtual polar axis.[14] When subjected to mechanical stress or vibration, this equilibrium within the crystal structure would be disrupted, resulting in an irregular arrangement of the dipoles and the generation of charges. Within the material, mechanical stress (stretching or compression) causes the charge balance to be disturbed and deforms the internal structure of the crystal. As a result, the positive and negative charges are separated because of the disruption of molecular neutrality, resulting in a corresponding surface charge density. When an external load is connected via electrodes, free charge transfer is induced in the external circuit.

To maximize the efficiency of mechanical signal collection, it is necessary to understand the mode in which PVDF converts the mechanical energy contained in the respiratory airflow into electrical output. We made a sample of PENG to evaluate the output characteristics, with a size of 2.0 cm × 0.8 cm × 0.01 cm. Then, we used a linear motor to drive the reference sample without contacts-separation, and recorded its output performance (Figures S1 and S2, Supporting Information). The results showed the open-circuit voltage (V_{OC}) was ≈2 V, while the short circuit current (I_{SC}) was ≈4 nA. We have developed a force-electric coupling model of the sample of PENG and simulated the electrical potential distribution before and after the deformation using the multi-physics field simulation software COMSOL (Figure S3, Supporting Information). It can be found that when the PENG is driven by breathing to undergo periodic deformation, the magnitude of the electrical potential generated by each part is positively correlated with the degree of deformation. Based on the results of the COMSOL simulation of the PENG potential distribution, we can speculate that the best collection of respiratory mechanics signals can be made when the PENG is fixed at the point where the maximum strain occurs in the respiratory drive component.

The PENG needs to be combined with a breath collection device to achieve the function of breath monitoring. Considering that masks have become a common tool and necessity in daily life, we chose the mask as the carrier for the PENG.

The gas valve of the mask is the part where the breathing airflow is concentrated (Figure 2b), so we integrated the PENG at the gas valve for respiratory parameters collection. The flexible gasket inside the valve is driven outwards by the airflow during exhalation, facilitating the exhalation process for the wearer, and retracts inwards during inhalation, closing the valve and blocking the entry of airborne dust or viruses, etc. The process causes a cyclical deformation of the PENG (Figure 2c). Combined with COMSOL simulation results, we designed three different PENG shapes for specific situations (Figure S4, Supporting Information). Using Kapton double-sided tape and aluminum adhesive tape, the PENG with specific shapes got fixed to the inner surface of the gasket and connected to the external circuit, respectively. We recorded the results of respiratory mechanics signal acquisition for different shapes of PENG consisting of 28 µm of PVDF, under the same conditions. The voltage outputs corresponding to the respiratory mechanics signals recorded by the oscilloscope are shown in Figure 2d. The tests were completed at a normal respiratory rate (16–20 breaths per minute). The PENGs corresponding to shapes 1, 2, and 3 produced peak output voltage signals of ≈-0.8, –0.4, and –0.1 V respectively when the subject inhaled, and peak output voltage signals of ≈1.7 V, 0.8 V and 0.4 V respectively when exhaling. The measurement results show that of the three shapes we have chosen, the PENG corresponding to shape 1 and shape 2, can produce a larger voltage output signal and the details of the output waveform corresponding to the breathing process got better retained. We also used three different thicknesses of PVDF (28, 52, and 110 µm) to prepare these two shapes of PENG and to test their output voltage signals (Figure S5, Supporting Information). The peak PENG output voltage of 28 µm in shape 1 is ≈1.7 V, much higher than the output of 52 and 110 µm. The output of the sample with 28 µm in shape 2 is also significantly higher than the other thicknesses. After comprehensive consideration, we determined the shape 1 PENG prepared with 28 µm PVDF as the mechanical signal-detecting part of the multi-parameter respiratory sensor.

Respiratory rate and patterns are important indicators for detecting health problems in the body as they provide information on how the cardiopulmonary system works.[15] The normal breathing rate for an adult at rest is 12–18 breaths per minute.[16] Abnormal breathing rates, such as slow breathing (abnormally slow) and rapid breathing (abnormally rapid), are warning signs of various underlying illnesses and psychological stress.[17] To verify the ability of the SMRS sensor to measure human breathing characteristics, we recorded five breathing patterns in real-time using a 28 µm shape 1 PENG, including sleep breathing, deep breathing, normal breathing, rapid breathing, and coughing (Figure 2e). It can be seen that the intervals between the peaks and amplitudes of the electrical signals generated differ for the different breathing behaviors. Deep breathing has the longest interval, while ragged breathing has the shortest interval. The reason is that the interval and amplitude are proportional to the period and the intensity of each breath, respectively. The magnitude of the positive output amplitude corresponds to the intensity of the exhalation, while the magnitude of the negative output amplitude corresponds to the intensity of the inhalation. It thus enables the respiratory sensor to distinguish between different breathing patterns without an external power supply.

2.2. Working Mechanism and Performance of Pyroelectric Part of SMRS

The pyroelectric effect refers to the phenomenon that temperature fluctuation with time changes produces corresponding electrical signals.[18] Some symmetrical dielectric materials can show this characteristic under the action of temperature. The working mechanism of the pyroelectric part of the SMRS is shown in **Figure 3**a. The properties of PyNG depend on the pyroelectric properties of poled PVDF films that polarize along the vertical direction of the membrane, which generates negative and positive charges on the upper and lower electrodes of the membrane, respectively. When the outside temperature changes from low to high, the dipole oscillates over a wide range of diffusion angles due to increased thermal motion. Then the polarization density of the PVDF film is reduced, resulting in a decrease of induced charges in the electrode. If connected a load between the bottom to the top electrodes, the electrons will be driven by the potential difference caused by the induced charges. However, the decrease in temperature increases the dipole moment in the PVDF film, which leads to an increase in polarization density and a reverse current in the external circuit.

Since the PVDF film used in the experiment is thin, which can be regarded as a uniform pyroelectric material, its temperature T is uniform at any time, and the surface charge and voltage of the pyroelectric output current generated by it can be determined by the following equation:[19]

$$I = pA\frac{dT}{dt} \tag{1}$$

$$Q = \int_{T_1}^{T_2} I dt = pA\Delta T \tag{2}$$

$$V = pt\Delta T/\varepsilon \tag{3}$$

where I is the pyroelectric current of the PVDF film, p is the pyroelectric coefficient (≈30 µC m^{-2} K), A is the variable temperature area of the PVDF, dT/dt is the rate of temperature change, Q is the pyroelectric charge, T_2 and T_1 represent the temperature at which the PVDF is heated up to and cooled down to respectively, and ΔT is the temperature range. V is the potential difference between the electrodes on both sides of the pyroelectric film, t is the film thickness, and is the dielectric constant of the PVDF film.

After understanding the principle of pyroelectricity in PVDF, the output of its pyroelectricity was tested under realistic conditions. The response of PVDF to temperature changes at rest was first tested using a standard rectangular sample prepared from 28 µm thickness of PVDF. A temperature-controlled heat source was periodically brought close to the sample at a room temperature of 20 °C (294 K), stabilized for 3 s and then moved away and cooled in the air for 7 s. Considering the temperature range in which people live in practical situations, we tested the temperature

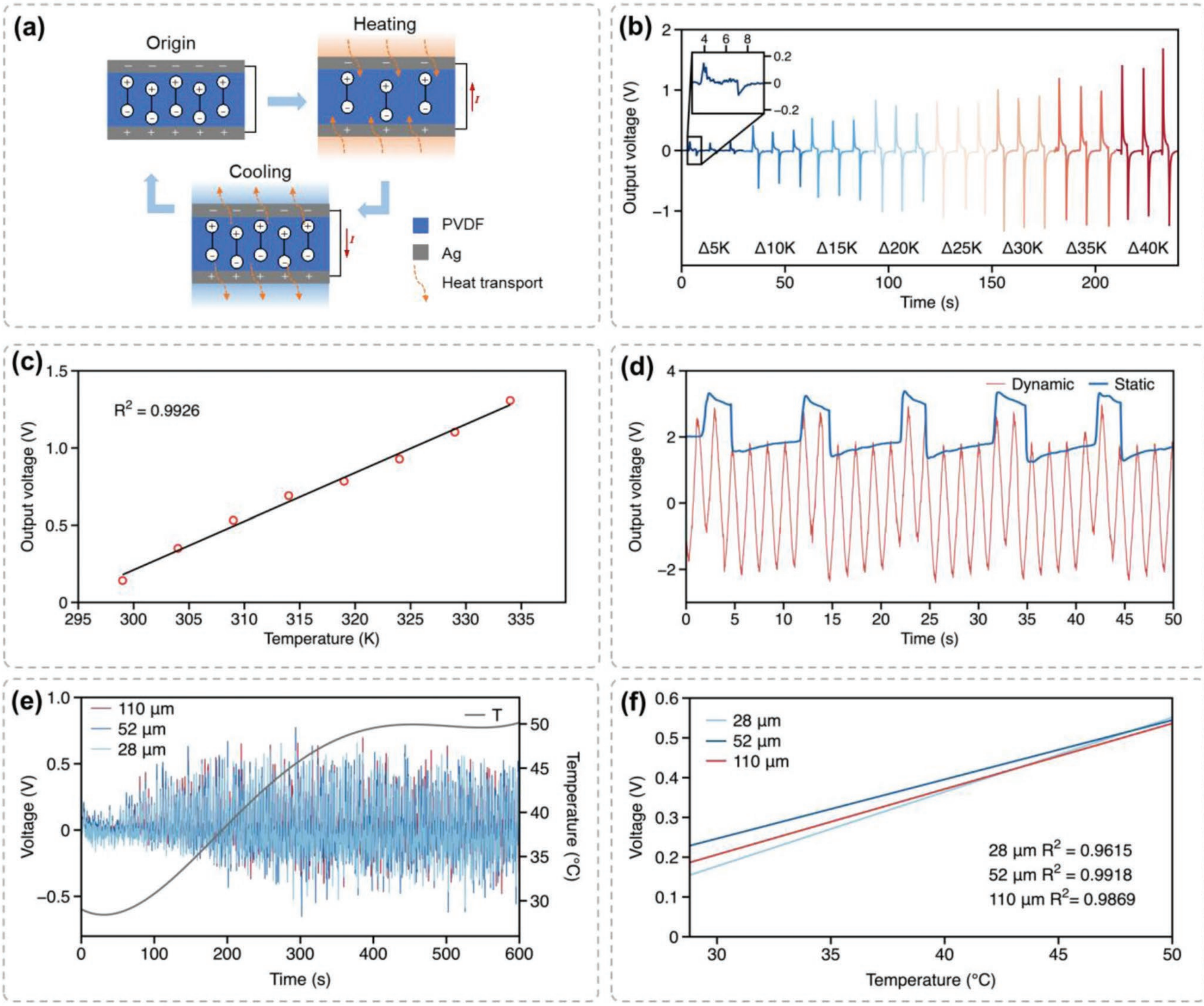

Figure 3. Working mechanism and electrical outputs of the PyNG based on the PVDF film. a) Schematic diagram of the PyNG. b) Static temperature response test results. c) Static pyroelectric response versus temperature fitting curve. d) Dynamic force-thermal response signals (the static line raised 2 V). e) Dynamic force-thermal response signal of the PyNG driven by airflow. f) Dynamic force-thermal response versus temperature fitting curve of PyNG driven by airflow.

difference between the heat source temperature (299–334 K) and the room temperature at 5, 10, 15, 20, 25, 30, 35, and 40 K. The pyroelectric output voltage signals of the PVDF films were tested. The results are shown in Figure 3b and show that the pyroelectric output of the PVDF film increases with increasing temperature difference at the same room temperature (294 K), which is consistent with the findings of the simulation analysis.

In the test results, the positive and negative voltage outputs correspond to the proximity and departure of the heat source, respectively, with a larger temperature difference corresponding to a larger absolute value of the pyroelectric output voltage. At a temperature difference of 40 K, the PVDF film produces an output voltage that is ≈10 times larger than at a temperature difference of 5 K. As can be seen from the waveform magnification in Figure 3b, both the positive and negative voltage outputs at the same temperature difference exhibit significant waveforms over the temperature range of the static temperature response test. In the temperature range of 5–40 K, the difference in temperature between one side of the PVDF film and the other side of the heat source is large, resulting in the largest potential difference. Three seconds later when both sides of the PVDF are heated to the same temperature, the temperature difference disappears and the potential difference becomes 0. When the heat source leaves, the temperature difference between the two sides of the PVDF film is reversed, resulting in the opposite voltage output. It can be seen that within the experimentally set temperature range (299–334 K), the positive and negative pyroelectric output voltage waveforms are the same, indicating that the PVDF film is sufficiently heated when the heat source is close, and the temperature change rate of the PVDF film surface is closer to that when it is heated in the process of returning to room temperature after leaving.

To explore the variation rule of the output electric signal of the temperature-sensitive unit corresponding to the temperature of the heat source, we used the average peak value of the output voltage at different heat source temperatures to fit the temperature. As shown in Figure 3c, the linear correlation coefficient R^2 of the output voltage-temperature fitting curve was 0.9926, indicating that the same initial temperature (294 K), within the temperature variation range of static temperature response test (299–334 K), the pyroelectric output voltage of PVDF film has a good linear relationship with temperature, which is consistent with Equation 3, indicating that the temperature sensitive unit has good application potential in self-powered temperature sensing.

Meanwhile, the dynamic mechanical-temperature response characteristics of the SMRS are also important, as well as the static temperature response characteristics. Therefore, we use an infrared torch (940 nm,5 W) as the heat source, in the use of linear motor drive standard sample of cyclic deformation occurred at the same time, the infrared flashlight is far away from the sample again, record the process of compound voltage output signal. Figure 3d shows the static and dynamic electrical output signal that PVDF standard samples produced with a constant temperature heat source (infrared flashlight) moving toward and away from it. It can be observed that in the dynamic process, PVDF generates a relatively stable piezoelectric output signal without temperature change, with a peak value of ≈2 V, which is consistent with the test results above. When the heat source is close to the output voltage increases, after leaving the recovery, with a response time of ≈500 ms (Figure S6, Supporting Information). By raising the temperature response signal in the static process by 2 V, it can be seen that the temperature response signal in the dynamic process is consistent with that in the static process. We also test the output voltage with a small step of the temperature of 0.9 °C (≈37.4–38.3 °C), and fit the baseline from the outputs of it (Figure S7, Supporting Information). The results illustrate that there are consistent alteration trends between the outputs of the PVDF device and the continuous temperature change. To measure the stability of the PVDF film under normal temperature and relatively higher humidity, we tested the outputs at 37 °C under 50% relative humidity at different points of time of 1, 5, 10, 20, 30, 40, 50 min and 1 h. The results in Figure S8 (Supporting Information) indicate that PVDF has good dynamic mechanical-temperature response performance and stability.

Then, we tested the dynamic mechanical-thermal response performance under airflow drive combined with temperature change (Figure S9, Supporting Information). Combining the temperature range in real-life situations, we tested the dynamic mechanical-temperature response of the PVDF-based flexible multimodal respiration sensor driven by airflow in the temperature range 29–50 °C (Figure 3e). It can be seen that the temperature around the device increases from 29 to 50 °C within 600 s. As the temperature increases, the output voltage of the breath sensor gradually increases. In this case, the magnitude of the electrical signal generated by the different thicknesses of PVDF varied, but the trend with temperature was more consistent. To determine the trend of the output signal, we extracted the peak values of the V_{OC} of different thicknesses of the SMRS (Figure S10, Supporting Information). It is clear from the graph that the peak values of the V_{OC} of the PVDF follow the trend of temperature change, rising rapidly before leveling off.

We fitted the average peak value of the output voltage to the temperature at different temperatures, and the results are shown in Figure 3f. The fitted output voltage peak-temperature curves are slightly different for different thicknesses, but all have a large linear correlation coefficient ($R^2 > 0.95$), indicating that the airflow-driven flexible multimodal respiration sensor has a good linear relationship between the peak values of the V_{OC} and temperature for temperature variations (29–50 °C). This result is consistent with the pyroelectric output results and corresponding equations under static conditions, indicating that the respiratory sensor is capable of outputting a dynamic mechanical-temperature response with good temperature signal detection under airflow conditions.

2.3. The Characterization and Performance of Acetone Sensing Part of SMRS

We prepared sodium-doped zinc oxide (Na:ZnO) nanoflowers (NFs) by a simple solution synthesis method at a low temperature of 40 °C as acetone gas-sensitive materials (**Figure 4**a).[20] Then, to be easily integrated with other units, we chose flexible PET IDEs with a line width and line pitch of 100 and 50 µm respectively, and coated Na:ZnO NFs on the surface (Figure S11, Supporting Information). The surface morphology was observed using field emission scanning electron microscopy (SEM), as shown in Figure 4b. The Na:ZnO particles combined with the surface of the IDEs are composed of nanosheet clusters with a flower-like structure, and the particle size is ≈2.7 µm as can be seen from the magnified view. The morphology of Na:ZnO NFs shows that it has a large specific surface area and may achieve higher sensitivity as a gas sensor. Figure S12 (Supporting Information) shows the EDS mapping results for different elements, demonstrating that the Na element has been doped into the ZnO material during the preparation process to form the Na:ZnO NFs. To further determine the crystal structure of the Na:ZnO NFs and to characterize whether the Na doping affects their crystal structure, the samples were analyzed by XRD. As shown in Figure 4c, all the diffraction peaks correspond well to the hexagonal fibrillated ZnO structure (JCPDS No. 36–1451) and the lattice constants $a = b = 3.253$ Å and $c = 5.211$ Å. These demonstrate that the Na:ZnO NFs are highly crystalline and that the effect of Na doping on the crystal structure is negligible.

We used a commercial gas-sensitive analysis system to evaluate the acetone sensing ability of the prepared gas-sensitive elements (Figure S13, Supporting Information). The response of the Na:ZnO NFs sensor to acetone gas concentrations from 1 to 200 ppm at room temperature during UV irradiation is shown in Figure 4d, with the magnification showing the response time corresponding to a 2 ppm acetone gas concentration. It can be seen that the response of the Na:ZnO NFs sensor is positively correlated with the acetone concentration. The sensor also exhibited a more pronounced gas response at 1 ppm, as well as fast response and recovery characteristics, with response and recovery times of 20 and 23 s respectively at

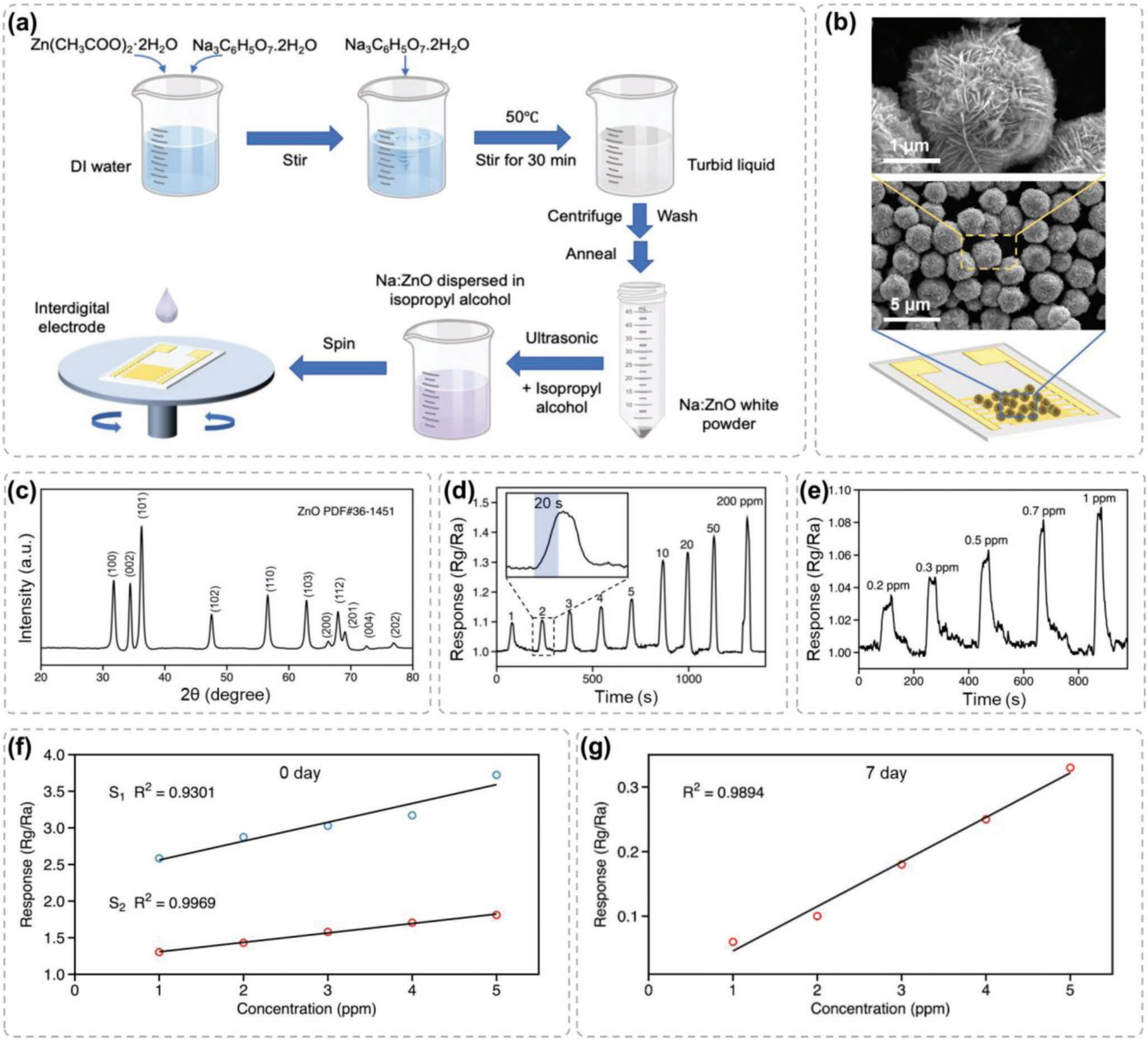

Figure 4. Preparation and characterization of acetone sensing unit based on Na:ZnO NFs. a) Schematic diagram of the preparation process of Na:ZnO NFs and gas-sensitive parts. b) SEM images and c) XRD patterns of the Na:ZnO NFs. Dynamic response of the Na:ZnO NFs gas molecular sensor to different concentrations of d) 1–200 ppm and e) 0.2-1 ppm acetone gas. f) Comparison of the response of the commercial acetone sensor (S1) and the Na:ZnO NFs sensor (S2) to low concentrations (1-5 ppm) of acetone gas. g) Acetone response of the Na:ZnO NFs sensor after one week of placement.

2 ppm. In Table S1 (Supporting Information), we compare the performance of some gas sensors in trace concentration of acetone. To further explore the minimum detection limits of the Na:ZnO NFs acetone sensor, we evaluated the response characteristics for acetone gas concentrations below the ppm level (Figure 4e). Here, we use the S value to evaluate the acetone response of the Na:ZnO NFs gas sensor. The gas response (S) is defined as $S = Rg/Ra$, in which the Ra and Rg are the resistance of the Na:ZnO NFs gas sensor before and after an exposure to acetone gas, respectively. As can be seen from the figures, the Na:ZnO NFs sensor can detect acetone gas at concentrations below ppm with a minimum detection limit of 0.2 ppm and an S value of 1.03 at this concentration.

To achieve differentiation between diabetics (exhaled acetone concentrations above 1.8 ppm) and healthy individuals (exhaled acetone concentrations below 0.8 ppm), gas-sensitive sensors need not only to have a more pronounced gas response in the low acetone concentration region, but also to have high reliability. We compared the acetone gas response of a commercial acetone sensor (S1) with that of a Na:ZnO NFs sensor (S2) in the low concentration region (1–5 ppm) (Figure 4f). It can be seen that the commercial acetone sensor has a higher response when the acetone concentration is low, but its linear correlation coefficient (R^2 = 0.9301) is significantly smaller than that of the Na:ZnO NFs sensor (R^2 = 0.9969). Besides, the ability to work stably after idle for long matters a lot to the gas sensor.

In Figure 4g, we can see that even though the acetone response dropped sharply, it remains a nice linear correlation coefficient ($R^2 = 0.9894$) with acetone concentration between 1 and 5 ppm. Since acetone concentrations in breath are generally low, and to perform disease diagnosis requires gas-sensitive sensors that can have a more accurate linear correlation at low concentrations. This result demonstrates that the Na:ZnO NFs sensor can more accurately differentiate between low concentrations of acetone and provides important clues for the development of respiratory sensor-based disease diagnosis and monitoring systems.

3. Conclusion

In conclusion, we propose a flexible multi-parameter respiration monitoring system that enables continuous monitoring of the mechanical, temperature, and molecular signals involved in exhaled gas of humans. It is composed of two flexible modular working parts, the first is a hybrid NG collecting mechanical and thermal signals, while the other is an acetone gas sensor for molecular signals monitoring. The flexible hybrid NG based on PVDF films can be driven by the airflow and differences in temperature during the respiratory process, thus generating corresponding electrical signals without an external power supply. The output waveforms of the respiration monitoring system correspond well with various breathing patterns, which shows promising applications for breathing pattern recognition. Meanwhile, there is a good linear correlation between the V_{OC} and ambient temperature. Na:ZnO NFs have been prepared by a simple solution synthesis method, which realized the detection of trace acetone around several ppm at room temperature while integrating with flexible interdigital electrodes. This combination of the self-powered respiratory sensor and flexible gas-sensitive elements is not only easy to use in daily life scenarios, but also enables the monitoring of multi-parameter respiratory signals, which provides new ideas for future research on life health monitoring and diagnostic systems.

4. Experimental Section

Materials: PVDF film (Shenzhen Zhimeikang Technology Co., Ltd.), Kapton tape (DuPont), face masks (9501V+, 3 M Co., Ltd., America), flexible polyethylene terephthalate (PET) interdigitated electrodes (IDEs, Huizhou Xinwenxiong Trading Co., Ltd.), and ultraviolet lamp beads (Shenzhen Ruibaoguang Technology Co., Ltd.) were purchased. Sodium hydroxide (NaOH), trisodium citrate dihydrate ($Na_3C_6H_5O_7{\cdot}2H_2O$), zinc acetate dihydrate ($Zn(CH_3COO)_2{\cdot}2H_2O$), and acetone were obtained from Aladdin Biochemical Technology Co., Ltd.

Fabrication of Piezoelectric and Pyroelectric Parts of SMRS: After cutting the PVDF to the desired shape, Kapton tape was applied to either side to act as a backing or fixation. Single-sided tape was used when PVDF films were prepared for stand-alone testing and double-sided tape was used when combined with other devices. As the piezoelectric and pyroelectric parts, the PVDF film was attached to a flexible gasket inside the gas valve of the commercial mask for the respiratory signals collecting.

Fabrication of Acetone Sensing Part of SMRS: NaOH was used as a precipitating and doping agent, and $Na_3C_6H_5O_7{\cdot}2H_2O$ as a chelating agent. 0.1 mol L^{-1} of $Zn(CH_3COO)_2{\cdot}2H_2O$ and 0.24 mol L^{-1} of $Na_3C_6H_5O_7{\cdot}2H_2O$ were dissolved in 30 mL of deionized water and stirred rapidly for 5 min to form a clear solution. The solution was then added with 0.03 mol of NaOH and stirred continuously for 30 min at 50 °C in a water bath heated. The white precipitate was collected and washed. Then, the white precipitate was annealed in an oven at 60 °C for 12 h to obtain the Na:ZnO NFs. The prepared white powder was dispersed in isopropanol. After that, flexible IDEs were fixed on the homogenizer, and a certain amount of the dispersion was suspended and coated on the surface and dried at 60 °C for 12 h.

Characterizations and Measurements of SMRS: Piezoelectric output performance testing of the PENG was achieved using a linear motor (60-R/30*120F, Teknor Linear Motors Co. Ltd., Suzhou). The open circuit voltage (V_{SC}) and short circuit current (I_{SC}) generated were recorded using Keithley 6517B electrometer (Tektronix) and Teledyne HD 4096 oscilloscope (LeCroy). Volunteer testers wear mask with SMRS and the mechanical signals generated by different breathing patterns were collected and recorded using Teledyne HD 4096 oscilloscope (LeCroy).

Using FEI field emission scanning electron microscope (Nova NanoSEM 450) with X-ray energy spectrometer (EDS) module to observe the microscopic morphology and the micro-regional energy spectral composition of Na:ZnO NFs. The synthesized Na:ZnO NFs powder samples were characterized by X-ray Diffraction (XRD) using an Xpert3 Powder X-ray diffractometer at 20°–80°. The performance of the acetone gas-sensitive part was measured using an intelligent gas-sensitive analysis system (CGS-1TP, Beijing Alite Technology Co., Ltd.).

The experiments involving human subjects had been performed with the full, informed consent of the volunteer, who was also a co-author of the manuscript. All experiments were approved by the Committee on Ethics of Beijing Institute of Nanoenergy and Nanosystems (A-2021006).

Supporting Information

Supporting Information is available from the Wiley Online Library or from the author.

Acknowledgements

This work was supported by the National Natural Science Foundation of China (61875015, T2125003, 32101117, U20A20390, and 11827803), the Strategic Priority Research Program of the Chinese Academy of Sciences (XDA16021101), the Beijing Natural Science Foundation (JQ20038, L212010), and the Fundamental Research Funds for the Central Universities.

Conflict of Interest

The authors declare no conflict of interest.

Data Availability Statement

The data that support the findings of this study are available from the corresponding author upon reasonable request.

Keywords

multi-parameters, nanogenerators, respiration sensors, self-powered

Received: September 15, 2022
Revised: December 11, 2022
Published online:

[1] a) A. T. Güntner, S. Abegg, K. Königstein, P. A. Gerber, A. Schmidt-Trucksäss, S. E. Pratsinis, *ACS Sens.* **2019**, *4*, 268; b) T. Bruderer, T. Gaisl, M. T. Gaugg, N. Nowak, B. Streckenbach, S. Muller, A. Moeller, M. Kohler, R. Zenobi, *Chem. Rev.* **2019**, *119*, 10803.

[2] Y. Su, G. Chen, C. Chen, Q. Gong, G. Xie, M. Yao, H. Tai, Y. Jiang, J. Chen, *Adv. Mater.* **2021**, *33*, 2101262.

[3] a) A. Amann, W. Miekisch, J. Schubert, B. Buszewski, T. Ligor, T. Jezierski, J. Pleil, T. Risby, *Annu. Rev. Anal. Chem.* **2014**, *7*, 455; b) H. L. Tai, S. Wang, Z. H. Duan, Y. D. Jiang, *Sensor Actuat B-Chem* **2020**, *318*, 128104.

[4] a) L. L. W. Chan, M. N. Anahtar, T. H. Ong, K. E. Hern, R. R. Kunz, S. N. Bhatia, *Nat. Nanotechnol.* **2020**, *15*, 792; b) W. Miekisch, J. K. Schubert, G. F. E. Noeldge-Schomburg, *Clin. Chim. Acta* **2004**, *347*, 25.

[5] a) P. L.e Maout, J. L. Wojkiewicz, N. Redon, C. Lahuec, F. Seguin, L. Dupont, S. Mikhaylov, Y. Noskov, N. Ogurtsov, A. Pud, *Sensor Actuat B-Chem* **2018**, *274*, 616; b) A. J. Engstler, T. Aumiller, C. Degen, M. Durr, E. Weiss, I. B. Maier, J. M. Schattenberg, C. J. Jin, C. Sellmann, I. Bergheim, *Gut* **2016**, *65*, 1564; c) A. W. Jones, *J Clin Forensic Med* **2000**, *7*, 48; d) D. Enko, G. Kriegshauser, *Clin. Biochem.* **2017**, *50*, 46; e) W. W. Li, Y. Liu, X. Y. Lu, Y. P. Huang, Y. Liu, S. Q. Cheng, Y. X. Duan, *J Breath Res* **2015**, *9*, 016005.

[6] a) R. Selyanchyn, S. Wakamatsu, K. Hayashi, S.-W. Lee, *Sensors* **2015**, *15*, 18834; b) T. Saidi, O. Zaim, M. Moufid, N. El Bari, R. Ionescu, B. Bouchikhi, *Sens. Actuators, B* **2018**, *257*, 178; c) M. Bhattacharjee, H. B. Nemade, D. Bandyopadhyay, *Biosens. Bioelectron.* **2017**, *94*, 544; d) H. Yan, S. Guo, F. Wu, P. Yu, H. Liu, Y. Li, L. Mao, *Angew. Chem., Int. Ed.* **2018**, *57*, 3922.

[7] R. Z. Luo, J. Y. Dai, J. P. Zhang, Z. Li, *Adv. Healthcare Mater.* **2021**, *10*, 2100557.

[8] L. Pan, C. Wang, H. Jin, J. Li, L. Yang, Y. Zheng, Y. Wen, B. H. Tan, X. J. Loh, X. Chen, *ACS Mater. Lett.* **2020**, *2*, 1178.

[9] A. Chen, A. J. Halton, R. D. Rhoades, J. C. Booth, X. Shi, X. Bu, N. Wu, J. Chae, *ACS Sens.* **2019**, *4*, 944.

[10] a) Z. Li, Q. Zheng, Z. L. Wang, Z. Li, *Res.-China* **2020**, 2020; b) Q. Zheng, Q. Z. Tang, Z. L. Wang, Z. Li, *Nat Rev Cardiol* **2021**, *18*, 7; c) J. Chen, Y. Huang, N. N. Zhang, H. Y. Zou, R. Y. Liu, C. Y. Tao, X. Fan, Z. L. Wang, *Nat. Energy* **2016**, *1*, 16138; d) B. Y. Yu, J. J. Duan, H. J. Cong, W. K. Xie, R. Liu, X. Y. Zhuang, H. Wang, B. Qi, M. Xu, Z. L. Wang, J. Zhou, *Science* **2020**, *370*, 342; e) Y. Yu, J. Nassar, C. H. Xu, J. H. Min, Y. R. Yang, A. Dai, R. Doshi, A. Huang, Y. Song, R. Gehlhar, A. D. Ames, W. Gao, *Sci Robot* **2020**, *5*, eaaz7946.

[11] a) Q. Zheng, H. Zhang, B. Shi, X. Xue, Z. Liu, Y. Jin, Y. Ma, Y. Zou, X. Wang, Z. An, W. Tang, W. Zhang, F. Yang, Y. Liu, X. Lang, Z. Xu, Z. Li, Z. L. Wang, *ACS Nano* **2016**, *10*, 6510; b) Q. Zheng, B. Shi, F. Fan, X. Wang, L. Yan, W. Yuan, S. Wang, H. Liu, Z. Li, Z. L. Wang, *Adv. Mater.* **2014**, *26*, 5851.

[12] a) J. Y. Dai, L. L. Li, B. J. Shi, Z. Li, *Biosens. Bioelectron.* **2021**, 194; b) F. R. Fan, W. Tang, Z. L. Wang, *Adv. Mater.* **2016**, *28*, 4283; c) T. Tat, A. Libanori, C. Au, A. Yau, J. Chen, *Biosens. Bioelectron.* **2021**, *171*, 112714; d) S. Wang, H. L. Tai, B. H. Liu, Z. H. Duan, Z. Yuan, H. Pan, Y. J. Su, G. Z. Xie, X. S. Du, Y. D. Jiang, *Nano Energy* **2019**, *58*, 312; e) H. Xue, Q. Yang, D. Y. Wang, W. J. Luo, W. Q. Wang, M. S. Lin, D. L. Liang, Q. M. Luo, *Nano Energy* **2017**, *38*, 147.

[13] X. L. Chen, J. Y. Shao, N. L. An, X. M. Li, H. M. Tian, C. Xu, Y. C. Ding, *J. Mater. Chem. C* **2015**, *3*, 11806.

[14] a) J. P. Lee, J. W. Lee, J. M. Baik, *Micromachines* **2018**, *9*, 532; b) M. H. You, X. X. Wang, X. Yan, J. Zhang, W. Z. Song, M. Yu, Z. Y. Fan, S. Ramakrishna, Y. Z. Long, *J. Mater. Chem. A* **2018**, *6*, 3500; c) N. Goonoo, A. Bhaw-Luximon, *Mater. Today Commun.* **2022**, *31*, 103491.

[15] T. Sengthipphany, S. Tretriluxana, K. Chitsakul, presented at 2014 7th Biomedical Engineering Int. Conf. (Bmeicon), Fukuoka, Japan, November **2014**.

[16] E. Allado, M. Poussel, J. Renno, A. Moussu, O. Hily, M. Temperelli, E. Albuisson, B. Chenuel, *J. Clin. Med.* **2022**, *11*, 3647.

[17] a) S. Kano, A. Yamamoto, A. Ishikawa, M. Fujii, *Ieee Eng Med Bio* **2019**, 3567; b) X. Zhang, J. W. Ai, R. P. Zou, B. Su, *ACS Appl. Mater. Interfaces* **2021**, *13*, 15727.

[18] A. Cuadras, M. Gasulla, V. Ferrari, *Sens. Actuators, A* **2010**, *158*, 132.

[19] Y. Yang, H. L. Zhang, G. Zhu, S. Lee, Z. H. Lin, Z. L. Wang, *ACS Nano* **2013**, *7*, 785.

[20] R. Jaisutti, M. Lee, J. Kim, S. Choi, T. J. Ha, J. Kim, H. Kim, S. K. Park, Y. H. Kim, *ACS Appl. Mater. Interfaces* **2017**, *9*, 8796.

